Journal of the Korean Ceramic Society
https://doi.org/10.1007/s43207-026-00653-y

ORIGINAL ARTICLE

Effect of the secondary phase content on the ferroelectric, piezoelectric, and dielectric properties of $0.96(K_{0.48}Na_{0.52})Li_{0.05}Nb_{0.95}Ta_{0.05}O_3$-$0.04BaZrO_3$ piezoceramics

Espiridión Martínez-Aguilar[1] · Orlando Hernández-Cristóbal[2] · H'Linh Hmŏk[3] · Rigoberto López-Juárez[1]

Received: 16 March 2026 / Revised: 28 May 2026 / Accepted: 1 July 2026
© The Author(s) 2026

Abstract
Lead-free KNN-based piezoceramics with different contents of secondary phase were synthesized via conventional solid-state method. The influence of the tungsten-bronze secondary phase on the ferroelectric, piezoelectric and dielectric properties was systematically investigated. The presence of the secondary phase significantly deteriorated the materials performance, reducing both piezoelectric and ferroelectric response. Specifically, the d_{33} increased from 142 pC/N for ceramics containing ~1.5 wt% of tungsten-bronze (TB) secondary phase to 203 pC/N for the KNLNT-BZ sample with less than 0.3% of TB phase. Despite the relatively low secondary-phase content (<2 wt%), the piezoelectric response decreased by near 34%, highlighting the strong sensitivity of KNN-based systems to phase purity. These findings confirm that strict control of secondary phases is essential to maximize the electromechanical performance of lead-free KNN piezoelectric ceramics.

Keywords Lead-free KNN piezoceramics · XRD analysis · Solid state synthesis · Ferroelectricity

1 Introduction

Lead is a major component of $PbZr_{1-x}Ti_xO_3$ (PZT) piezoceramics, which remain widely used in electronic devices such as actuators, sensors, motors and transformers due to their excellent electromechanical performance [1–3]. However, increasing environmental and health concerns associated with lead-containing compounds, together with regulations such as the Restriction of Hazardous Substances (RoHS) directive [4], have stimulated extensive research into lead-free piezoelectric alternatives during the last two decades [5–15]. Among the different candidates investigated, $BaTiO_3$ (BT) [16–17], $Bi_{0.5}Na_{0.5}TiO_3$ (BNT) [18–19] and $K_{0.5}Na_{0.5}NbO_3$ (KNN)-based systems [20–21] have attracted particular attention. In particular, KNN-based piezoceramics are considered one of the most promising substitutes for PZT because of their high Curie temperature, good piezoelectric response, and compositional flexibility [2, 21–23].

For improving the electrical performance of KNN-based ceramics, extensive efforts have been devoted to both compositional engineering and processing optimization. The first strategy involves compositional modification through doping at the A and B-sites of the perovskite-type structure using elements such as Li, Ba, Ca, and Sr at the A-site, or Sb, Ta, Zr, and Sc at the B-site, aiming to tailor phase coexistence, lattice distortion, and domain mobility [1, 5, 7, 15, 22–27]. The second strategy focuses on improving densification and minimizing alkali loss through advanced sintering techniques such as Spark Plasma Sintering (SPS)

✉ Rigoberto López-Juárez
rlopez@iim.unam.mx

1 Unidad Morelia del Instituto de Investigaciones en Materiales, Universidad Nacional Autónoma de México, Antigua Carretera a Pátzcuaro No. 8701, Col. Ex Hacienda de San José de la Huerta, Morelia C.P. 58190, Michoacán, México

2 Escuela Nacional de Estudios Superiores Unidad Morelia, Universidad Nacional Autónoma de México, Antigua Carretera a Pátzcuaro No. 8701, Col. Ex Hacienda de San José de la Huerta, Morelia C.P. 58190, Michoacán, México

3 SEHCITI-Centro de Nanociencias y Nanotecnología, Universidad Nacional Autónoma de México, km 107 Carretera Tijuana-Ensenada, AP 14, Ensenada 22860, B. C, México

Published online: 27 July 2026

[28–29], multi-step sintering [30–31], cold sintering [32–33], and Sintering in Reducing Atmosphere (SRA) [34]. Likewise, different synthesis techniques have been developed to obtain highly crystalline powders avoiding the secondary phases before the sintering stage [35–39].

Among the various KNN-based systems, compositions co-modified with Li, Ta, Ba, and Zr, such as the $0.96(K_{0.48}Na_{0.52})_{0.95}Li_{0.05}Nb_{0.95}Ta_{0.05}O_3 - 0.04BaZrO_3$ (KNLNT-BZ) system are of particular technological interest due to their enhanced piezoelectric performance. These compositions are designed to exhibit a polymorphic phase transition (PPT) near room temperature, where the coexistence of orthorhombic and tetragonal phases promotes high electromechanical response through enhanced polarization rotation and domain-wall mobility. However, their complex stoichiometry and the presence of multiple volatile alkali species make them especially susceptible to stoichiometric deviations and secondary phase formation during high-temperature processing. As a result, KNLNT-BZ ceramics constitute a model system for investigating the relationship between alkali compensation, phase evolution, and electrical performance.

Despite these efforts, the volatilization of alkali elements during high temperature processing remains one of the principal limitations of KNN-based systems. Alkali loss generates a deviation from stoichiometry, promotes the formation of cation vacancies, and frequently induces secondary phases, particularly tetragonal tungsten bronze (TB)-type structures [1, 22–23, 26]. To mitigate this issue, excess K/Na precursors are commonly introduced into the starting composition to compensate for alkali volatilization during sintering. However, achieving an appropriate compensation level remains a critical challenge. Insufficient compensation cannot effectively suppress alkali deficiency, whereas excessive compensation promotes the formation of TB secondary phases. Consequently, the final microstructure and functional performance of KNN ceramics are strongly governed by the balance between alkali volatilization and compensation.

Although TB secondary phases are generally associated with degraded electrical performance in KNN-based ceramics, most previous studies have discussed this effect only qualitatively. In many cases, the deterioration of electrical properties is merely reported once secondary phases are detected, without quantitatively correlating the degree of alkali compensation with the resulting TB phase fraction. Furthermore, the combined influence of the TB phase on dielectric, ferroelectric, piezoelectric, and particularly fatigue behavior remains insufficiently understood. Therefore, a quantitative understanding of how alkali compensation governs TB phase formation and consequently affects the functional properties of KNN ceramics is still lacking.

In this work, a processing centered approach is adopted to systematically investigate the influence of K/Na compensation on the formation of TB secondary phases and the resulting electrical performance of KNLNT-BZ piezoceramics. By carefully controlling the alkali compensator ratio, different fractions of the TB phase are systematically induced through controlled alkali compensation, and quantitatively analyzed by Rietveld refinement. The relationship between alkali compensation, phase evolution, microstructure, and functional properties, including dielectric, ferroelectric, piezoelectric, and fatigue behavior, is established in order to identify the optimal compensation window that effectively suppresses alkali deficiency while minimizing TB secondary phases formation and maximizing the long-term electromechanical performance of KNLNT-BZ ceramics.

2 Experimental

The $0.96(K_{0.48}Na_{0.52})_{0.95}Li_{0.05}Nb_{0.95}Ta_{0.05}O_3$-$0.04BaZrO_3$ piezoelectric ceramics were prepared using a conventional solid-state method. The starting raw materials were Na_2CO_3 (Merck, 99.5%), Li_2CO_3 (Merck, 99.99%), K_2CO_3 (Merck, 99.2%), Nb_2O_5 (Merck, 99.9%), Ta_2O_5 (Merck, 99.99%), $BaCO_3$ (Merck, 99.8%), and ZrO_2 (Merck, 99%). To investigate the evolution of secondary phase, additional samples containing 0.6 and 0.8 mol% excess of alkaline elements were prepared.

All reagents were dried at 170 °C for 4 h to eliminate absorbed moisture. The powders were then weighed according to the stoichiometric formula and homogenized in an agate mortar and pestle using acetone as a dispersing medium. The mixed powders were calcined at 850 °C for 3 h in air to promote phase formation. Then, the calcined powders were ball milled for 16 h in a plastic jar with zirconia grinding media and absolute ethanol, followed by drying at 100 °C for 4 h. Disks samples of 13 mm in diameter and 1 mm of thickness were fabricated by uniaxial pressing at 200 MPa. The pellets were then sintered at 1150–1160 °C for 3 h in air using a high temperature furnace (MTI).

The bulk density of the sintered samples was measured using the Archimedes method. Crystalline structure was assessed by X-ray diffraction (Bruker D2-phaser diffractometer, $k_{\alpha1} = 1.5406$ Å, $k_{\alpha2} = 1.54439$ Å, $k_{\alpha2}/k_{\alpha1} = 0.5$) and the diffraction patterns were refined using the Rietveld method implemented in the Fullprof suite software. Microstructural observations, both before and after polishing, were carried out using scanning electron microscopy (SEM, JEOL JSM-IT300HR). The average gain size was determined by the linear interception method with the ImageJ software.

For electrical characterization, both surfaces of the sintered disks were coated with silver paste and fired at 600 °C

for 30 min to form electrodes. The samples were poled under a DC electric field of 4 kV/mm at room temperature for 30 min. Piezoelectric coefficients (d_{33}) were measured after 24 h of the poling process (PolyK d_{33}-meter). For measuring all remaining piezoelectric parameters like d_{31}, k_p, k_{31}, etc., the impedance spectra were fitted with the aid of an iterative method, which has been published elsewhere [40–41]. Ferroelectric hysteresis loops were recorded at 10 Hz using a Radiant ferroelectric tester (RT66C). The dielectric permittivity was measured from room temperature to 550 °C with a precision impedance analyzer (Agilent 4294 A). To evaluate the thermal stability of the piezoelectric response, the poled samples were annealed at temperatures ranging from 75 to 450 °C in 50 °C increments and maintained for 1 h, followed by cooling to room temperature to measuring the remanent d_{33} values.

3 Results and discussion

3.1 Crystal structure

The X-ray diffraction (XRD) patterns presented in Fig. 1 reveal the presence of a secondary phase in the sample without excess alkaline elements, and in those containing 0.6 and 0.8 mol% added. This behavior is frequently reported in KNN-based lead-free related ceramics and is commonly attributed to the volatilization of alkaline species during high temperature processing, with sodium exhibiting the highest volatilization rate [1]. Such compositional deviations favor the formation of non-polar phases. The detected secondary phase was identified as $K_{2.6}Nb_{11.6}O_{30}$ (ICDD: 01-073-7471), which crystallizes in the tetragonal space group *P4/mbm* (#127) and belongs to the tungsten-bronze structural family [23–24, 26].

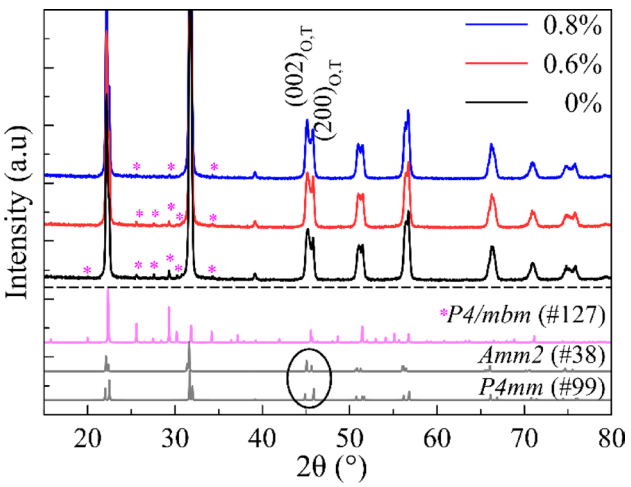


Fig. 1 The X-ray diffraction patterns of the $0.96(K_{0.48}Na_{0.52})_{0.95}Li_{0.05}Nb_{0.95}Ta_{0.05}O_3$-$0.04BaZrO_3$ ceramics with different amounts of excess alkaline elements. The most probable space groups describing the diffraction data are indicated at the bottom of the figure

For further quantification of the secondary phase and the ferroelectric phases present in the samples, Rietveld refinement was carried out using the Fullprof suite [42]. The structural model was tested considering orthorhombic (*Amm2* #38) and tetragonal (*P4mm* #99) symmetries. Although the refinement was performed over the entire diffraction range, special attention was paid to the pseudocubic {200} reflection located near 45°, since this region is highly sensitive to symmetry changes and allows discrimination between orthorhombic and tetragonal distortions. When the intensity ratio of the (002)/(200) reflections approaches 2:1, the structure is predominantly orthorhombic; if the ratio reverses to 1:2, a tetragonal phase dominates. A ratio close to 1:1 indicates coexistence of both orthorhombic and tetragonal phases, characteristic of a *PPT* region, which is known to enhance electromechanical response [9, 11, 22, 43].

The Rietveld refinement results for samples containing 0, 0.6 and 0.8 mol% of excess alkaline elements (EAE) are displayed in Fig. 2. Quantitative phase analysis shows that the sample without EAE consists of 81.45 wt% (±1.53%) orthorhombic phase, 16.71 wt% (±0.23%) tetragonal phase, and 1.84 wt% (±0.07%) TB secondary phase. Upon introducing 0.6 mol% EAE, the amount of the secondary phase decreases to 1.53 wt% (±0.08), indicating partial suppression of its formation. For the composition with 0.8 mol% EAE, the amount of the TB phase decreases drastically to approximately 0.22 wt%, indicating that alkaline compensation suppresses, although does not completely eliminate, the formation of the secondary phase, suggesting that the alkaline compensation effectively stabilizes the perovskite lattice.

Regarding the ferroelectric phases, the orthorhombic fraction remains close in magnitude across the three compositions, 81.45, 84.09 and 71.68 wt% for 0, 0.6 and 0.8 mol% EAE, respectively. In contrast, the tetragonal phase remains nearly unchanged for 0 and 0.6 mol% EAE (16.71 and 14.38 wt%), but increases significantly to 28.09 wt% in the 0.8 mol% EAE sample. This evolution indicates that alkaline compensation not only suppresses the tungsten-bronze phase but also shifts the orthorhombic-tetragonal balance toward a stronger phase coexistence. Such structural tuning is expected to play a key role in the enhancement of piezoelectric performance as discussed in Sect. 3.6.

3.2 Microstructure and grain-size evolution

To elucidate the spatial distribution of the secondary phases and its influence on microstructural development, the KNLNT-BZ ceramics were examined by scanning electronic microscopy (SEM), as shown in Fig. 3. All

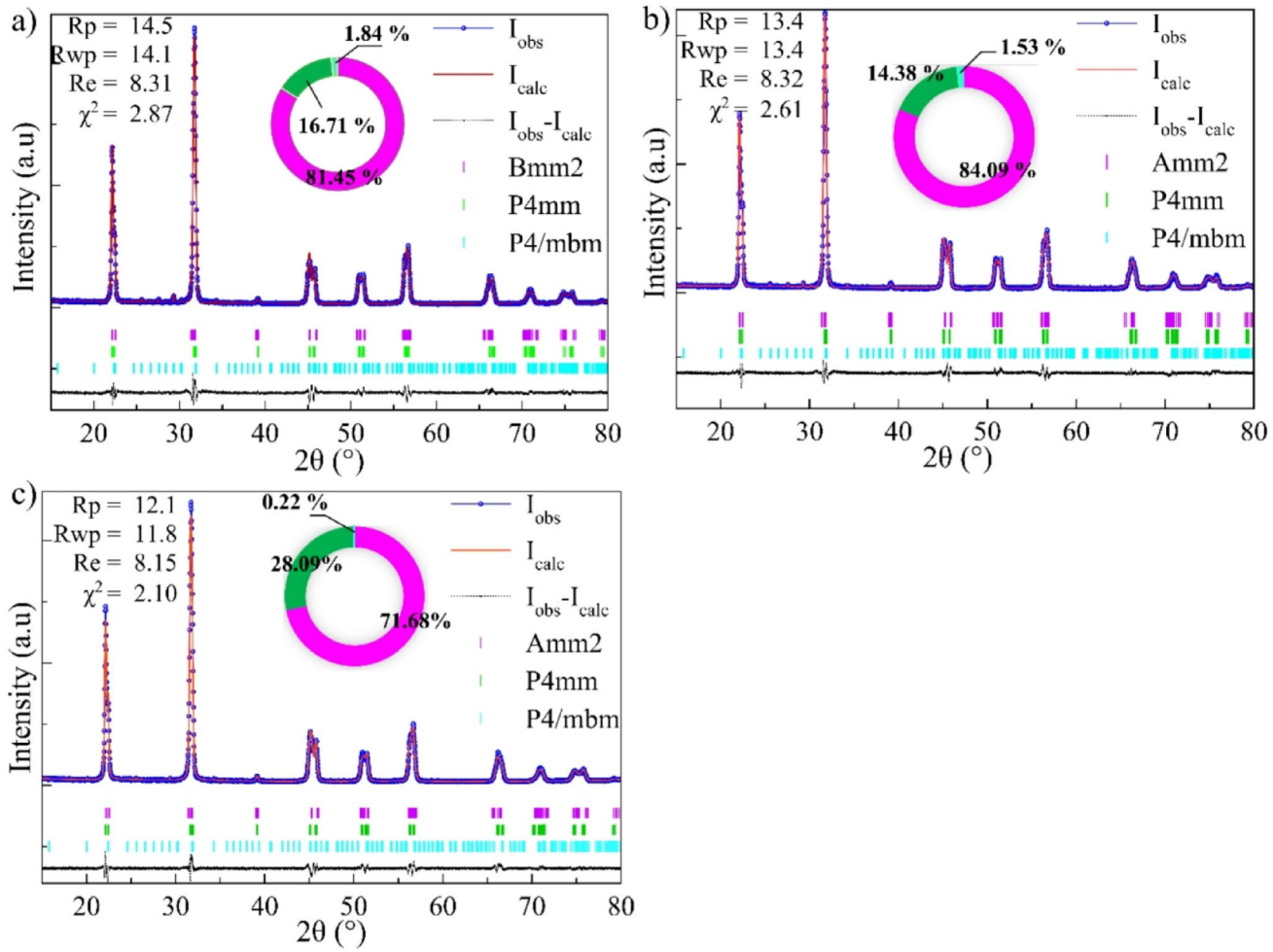


Fig. 2 Rietveld refinement profiles of the samples with (**a**) 0, (**b**) 0.6 and (**c**) 0.8 mol% excess alkali elements

compositions exhibit dense microstructures with well-developed grains and clean grains boundaries. The densities, measured by the Archimedes method are 4.57 g/cm^3, 4.58 g/cm^3, and 4.60 g/cm^3 for the 0, 0.6 and 0.8 mol% EAE compositions, respectively, indicating that the conventional solid-state route achieved adequate densification regardless of the alkali excess.

A clear difference in grain size is observed among the samples. The compositions with 0 and 0.6 mol% EAE display comparatively larger grains, whereas the sample with 0.8 mol% EAE shows a noticeably finer microstructure. The average grain sizes determined from SEM micrographs using ImageJ software are 1.47 µm, 1.48 µm and 1.31 µm for the 0, 0.6 and 0.8 mol% EAE compositions, respectively. This behavior can be correlated with the phase evolution identified by XRD Rietveld analysis. In the compositions containing higher amounts of the TB secondary phase, this phase likely acts as a transient liquid or diffusion enhancer during sintering, promoting mass transport and facilitating grain growth, as previously reported for KNN-based systems [22]. When the alkali excess increases to 0.8 mol%, the suppression of the TB phase removes this growth-assisting effect. At the same time, compensation through EAE reduces the concentration of vacancies at sites A, which limits cation diffusion and leads to restricted grain growth. Despite structural variations, all compositions show a similar density, allowing subsequent differences in functional behavior to be discussed, in terms of phase composition and defect-related effects.

3.3 Chemical analysis of KNLNT-BZ samples

To further clarify the chemical nature and spatial distribution of the secondary phase, Scanning Electron Microscopy (SEM) was used to examine polished ceramic surfaces in backscattered electron (BSE) mode, coupled with energy-dispersive X-ray spectroscopy (EDS). Figure 4 shows the BSE micrograph of the sample without excess alkaline elements (0% EAE). In BSE imaging, the secondary phase appears as bright, rectangular-shaped regions uniformly

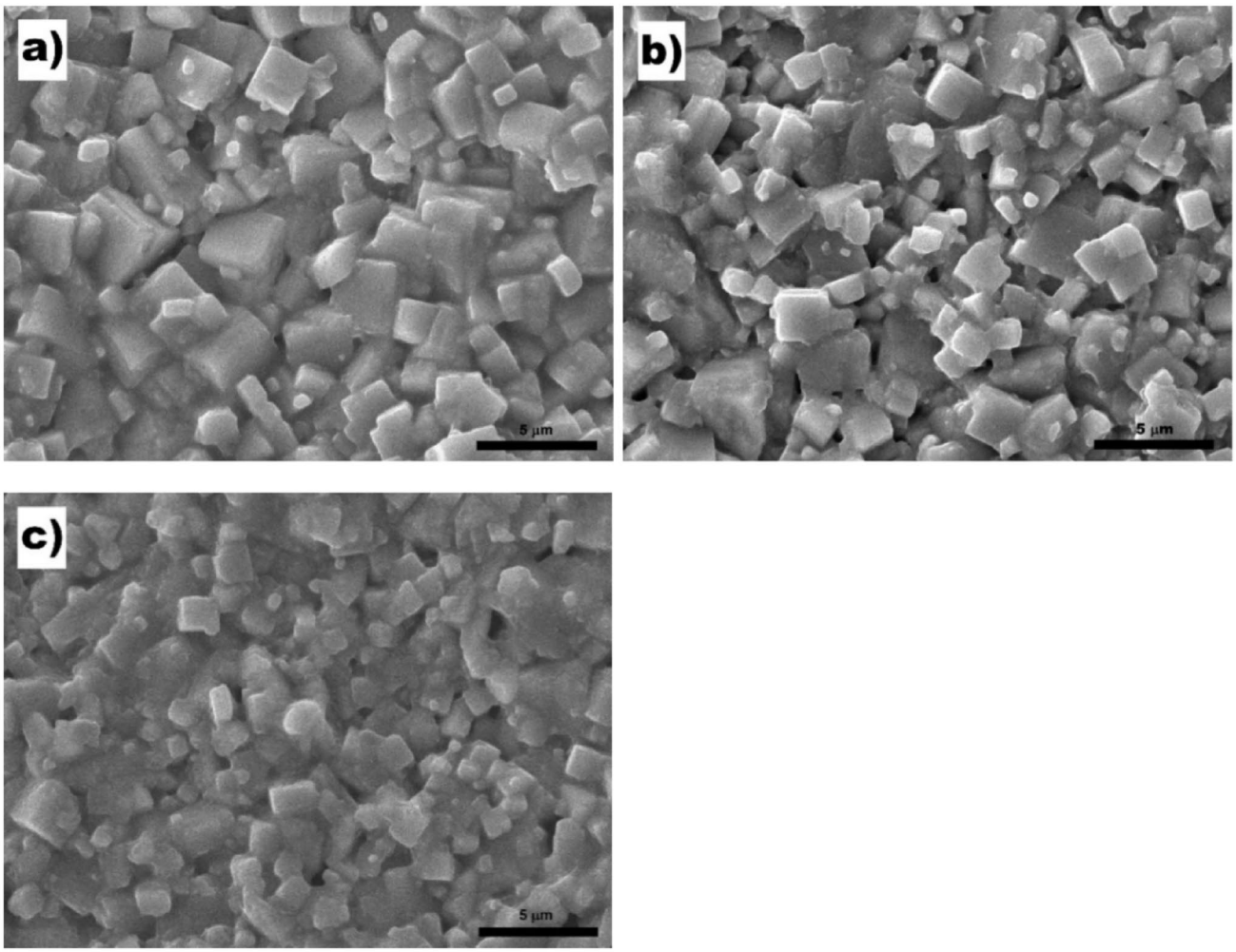


Fig. 3 SEM images of KNLNT-BZ ceramics with (**a**) 0%, (**b**) 0.6% and (**c**) 0.8 mol% EAE

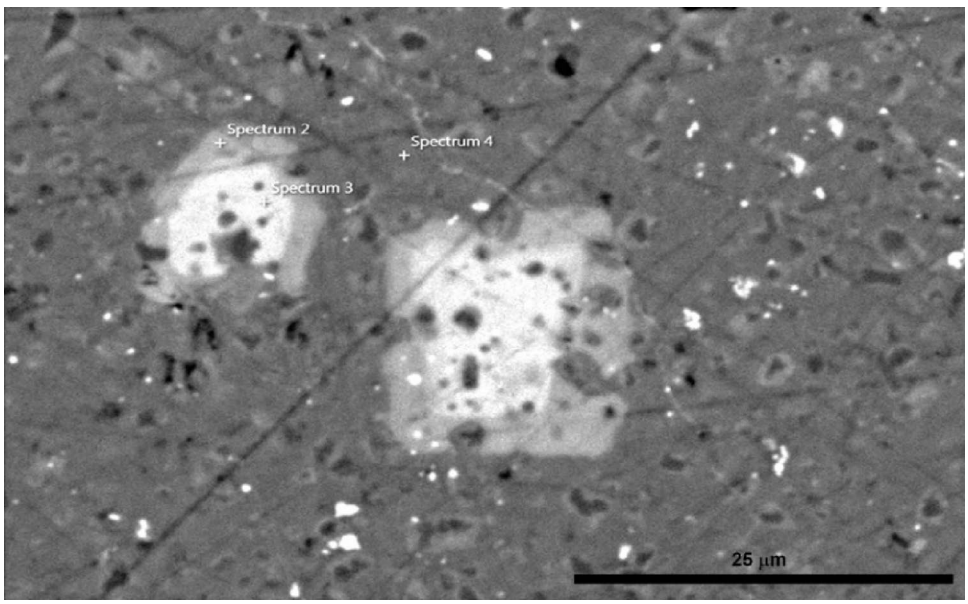


Fig. 4 SEM image (backscattered electron) of the polished surface of the sample without alkali excess

distributed within the matrix, and the brightest regions (points) correspond to high Ta concentrations, the heaviest element in the system under study, which occurs for all three systems with EAE (See supplementary material).

Table 1 summarizes the EDS point analyses performed at three representative regions: the outer region of the secondary phase (Spectrum 2), its inner region (Spectrum 3), and the surrounding matrix corresponding to the main perovskite phase (Spectrum 4). The compositional contrast between the secondary phase and the matrix is evident.

For the perovskite matrix (Spectrum 4), a probable local stoichiometry was estimated by normalizing the A and B site cations (Eqs S1-S3). It is important to note that EDS analysis provides reliable semi-quantitative information of heavy element (Na, K, Nb, Ta, Ba, Zr), but quantification of light elements is subject to significant uncertainties due to absorption effects, surface roughness, and other factors. Therefore, while the oxygen content values reported in Table 1 are listed as completeness, they should not be interpreted as accurate measure of the absolute oxygen stoichiometry. The resulting approximate formula is: $(K_{0.455}Na_{0.422}Ba_{0.032}Li_{0.048})(Nb_{0.93}Ta_{0.038}Zr_{0.0328})O_{(3-\delta)}$, with $\delta \approx 0.02$, which shows an approximate 10% deficiency of Na and K relative to the nominal stoichiometry, confirming alkali volatilization during sintering. Although EDS does not provide reliable quantitative determination of oxygen content, the measured cationic trends clearly indicate that alkali deficiencies develop locally within the ceramic matrix.

In contrast, the outer and inner regions of the secondary phase exhibit pronounced alkali depletion and Ba/Zr enrichment. The estimated local formulas of spectrum 2 (outer secondary phase) and spectrum 3 (inner secondary phase) are: $(K_{0.352}Na_{0.195}Ba_{0.096}Li_{0.048})(Nb_{0.902}Ta_{0.049}Zr_{0.048})O_{(3-\delta)}$, with $\delta \approx 0.132$, and $(K_{0.214}Na_{0.109}Ba_{0.202}Li_{0.048})(Nb_{0.879}Ta_{0.061}Zr_{0.060})O_{(3-\delta)}$, with $\delta \approx 0.530$, respectively. These results clearly demonstrate significant Na and K deficiency within the secondary phase where Ba partially occupies the A-site positions. This substitution alters the local charge balance, which may favor the formation of charge-compensating defects, as commonly observed in alkali-deficient KNN-based systems [44]. The compositional gradient between outer and inner regions suggests chemical segregation during solid-state diffusion, reinforcing the interpretation that the TB-type phase nucleates under alkali-deficient conditions.

Table 1 EDS point-analysis results (atomic %) for the sample without excess alkaline elements. EDS analysis is used for qualitative and semi-quantitative comparison of compositions between the matrix and secondary phases

Element	Spectrum 2 (Outer secondary phase)	Spectrum 3 (Inner secondary phase)	Spectrum 4 (Perovskite matrix)
O	62.97	63.17	57.98
Na	4.39	2.63	9.28
K	7.93	5.18	10.01
Zr	1.10	1.46	0.72
Nb	20.33	21.23	20.47
Ba	2.17	4.87	0.71
Ta	1.11	1.47	0.82
Total:	100.0	100.0	100.0

For the 0.6 mol% EAE composition, similar qualitative features were observed. Chemical segregation was identified from line-scan EDS profiles (Fig. 5); upon entering the bright zone of the secondary phase (Spectrum 2 on Figure S1 and Table S1), the Ba and Zr intensities increase, while K and Na signals decrease by approximately 64%. The corresponding estimated composition $(K_{0.328}Na_{0.117}Ba_{0.115}Li_{0.048})(Nb_{0.91}Ta_{0.033}Zr_{0.053})O_{(3-\delta)}$, with $\delta \approx 0.52$ indicates that moderate alkali enrichment does not completely suppress secondary phase formation but reduces its fraction and slightly alters its interfacial chemistry.

Importantly, these results suggest that the primary role of alkali excess is not to fundamentally alter the chemistry of the perovskite lattice, but rather to compensate for volatilization-induced A-site vacancies, thereby stabilizing the matrix and progressively reducing the volume fraction of TB phase. The chemical homogenization achieved at higher EAE levels correlates directly with the structural trends observed by Rietveld refinement and the grain-size evolution discussed in Sect. 3.2.

Given the known sensitivity of dielectric and ferroelectric properties to compositional heterogeneity and phase coexistence, the influence of this microstructure on the dielectric response are examined in the following section.

3.4 Dielectric properties

Figure 6 shows the temperature dependence of the relative permittivity (ϵ_r) and dielectric loss ($tan\delta$) for KNLNT-BZ ceramics containing 0, 0.6, and 0.8 mol% EAE. All compositions exhibit a broad and asymmetric dielectric anomaly near 220 °C, indicating a structurally frustrated transition driven by local chemical heterogeneity and competition between orthorhombic and tetragonal polar phases (O-T).

The O-T transition temperature, determined from the inflection point of the permittivity curve using the condition $d^2\epsilon'/dT^2 = 0$, lies in the range 211–222 °C (Table 3). The diffuse character of this transition is consistent with the structural analysis. Such coexistence, combined with nanoscale compositional heterogeneity evidenced by SEM-EDS analysis, results in a distribution of local transition temperatures as commonly observed in chemically disorder relaxor ferroelectrics [45–52] rather than a single sharp instability. The excess of Ba and enrichment in alkali-deficient

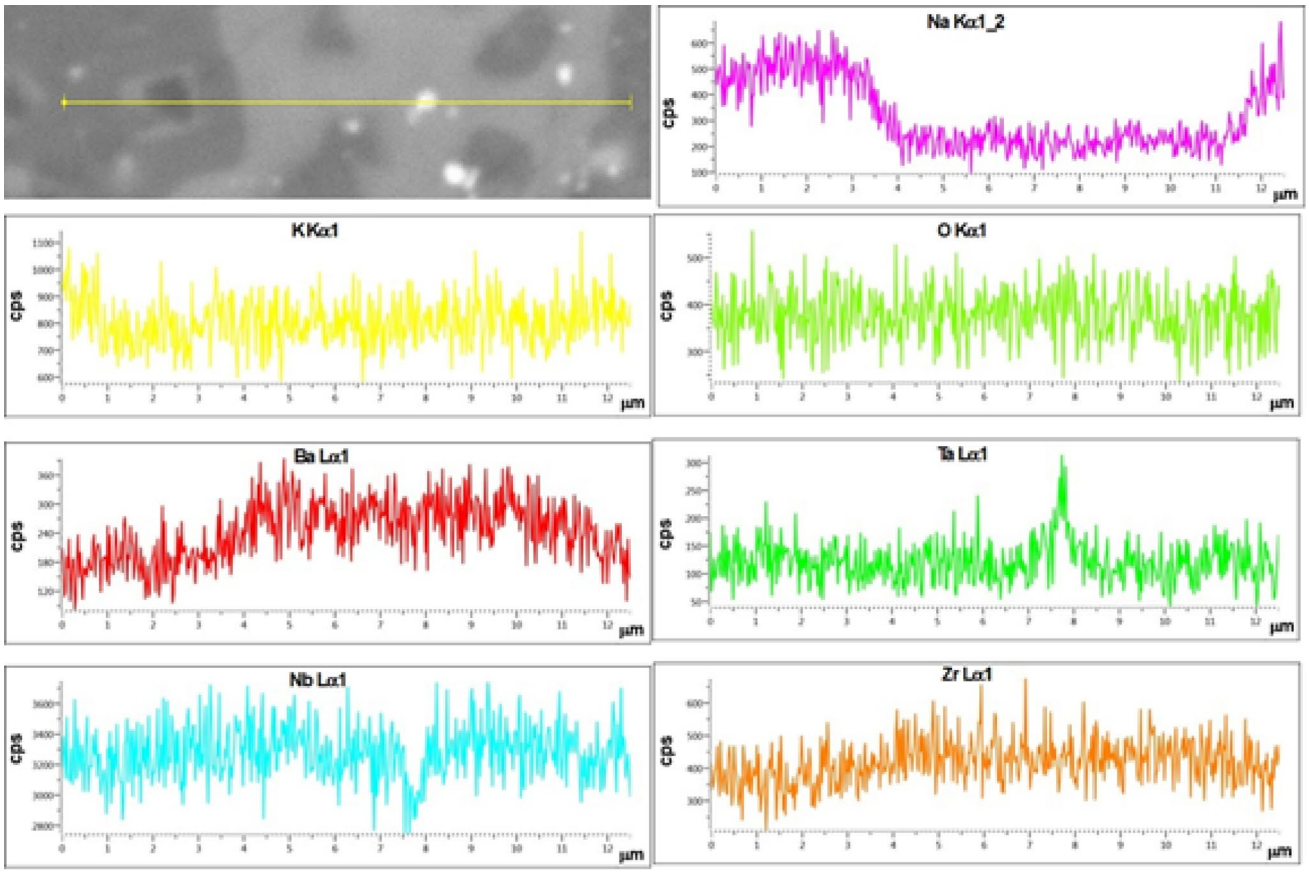


Fig. 5 EDS line-scan analysis across a representative secondary-phase region for alkali 0.6%, displaying elemental intensity profiles (counts per second, cps) for the primary constituent elements

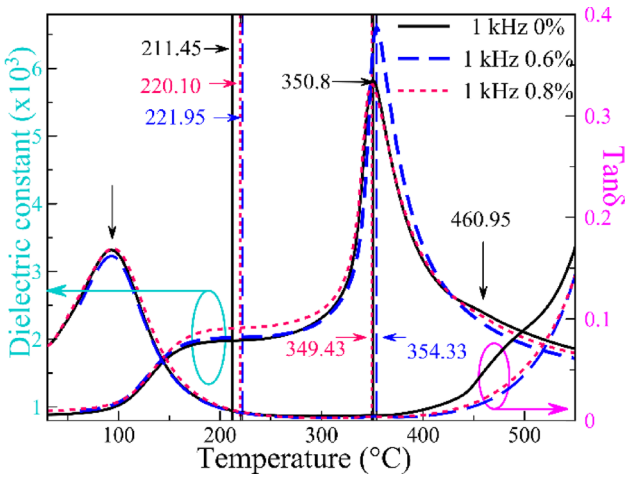


Fig. 6 Temperature-dependent relative permittivity and dielectric loss at 1 kHz for KNLNT-BZ ceramics containing 0, 0.6, and 0.8 mol% EAE

regions, together with Na/K vacancies, introduces local random electric fields and strain fluctuations. Consequently, the dielectric anomaly becomes broadened and slightly shifts depending on EAE content, reflecting the competition between long-range ferroelectric order and local structural disorder.

On the other hand, the dielectric loss curves (Figs. 6 and Figure S2) indicate that dipolar relaxation begins near 95 °C. With increasing measurement frequency, the loss maxima shift toward higher temperatures, demonstrating clear frequency dispersion. This behavior is characteristic of relaxor ferroelectrics and is commonly associated with the presence of polar nanoregions (PNRs), where polarization fluctuates between multiple equivalent orientations, giving rise to local fluctuations [48–52], consistent with the presence of secondary phases centrosymmetric observed in Sect. 3.2 and 3.3.

The Curie temperature (T_C), determined from the maximum of $\epsilon_r(T)$, lies between 349 and 354 °C for all compositions (Table 2), confirming that the intrinsic ferroelectric-paraelectric transition remains relatively stable despite alkali non-stoichiometry. Above T_C, a significant increase in $tan\delta$ is observed, particularly pronounced for the stoichiometric composition (0% EAE). This behavior is attributed to thermally activated hopping conduction mechanism associated with oxygen and alkali vacancies generated during sintering, in agreement with the SEM-EDS

Table 2 Dielectric transition temperatures and Curie–Weiss parameters of KNLNT-BZ ceramics with controlled alkali non-stoichiometry

Sample	T_{O-T} (°C)	T_c (°C)	ϵ_r (*r.t*)	ϵ_m	C (10^5 K)	γ
0%	211.45	350.80	887.58	5822.357	3.392	1.44
0.6%	221.95	354.33	914.22	6604.790	3.365	1.40
0.8%	220.10	349.53	941.85	5768.896	2.946	1.49

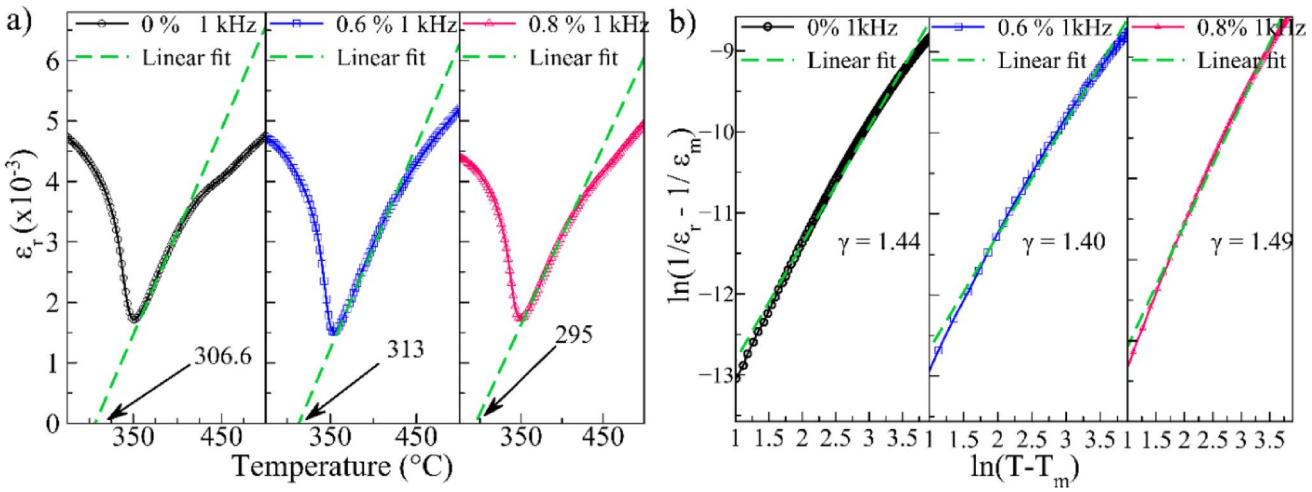


Fig. 7 (**a**) Curie-Weiss and (**b**) modified Curie-Weiss fit to the dielectric permittivity of KNLNT-BZ ceramics containing 0, 0.6 and 0.8 mol% EAE

observations and previous reports [46–49]. Additionally, a secondary dielectric anomaly appears near 460 °C, clearly within the paraelectric region. Its extrinsic origin is associated with the presence of TB phase, which is attenuated with increasing alkali excess. The behavior is consistent with previous reports on alkali-deficient KNN-based systems [11, 22, 42, 51, 53–54], where tungsten-bronze-type phases associated with Ba/Zr enrichment produce additional dielectric contributions at high temperatures. Therefore, the anomaly near 460 °C is attributed to the dielectric response of the TB secondary phase rather than an intrinsic ferroelectric transition.

To further describe the dielectric behavior, the permittivity data were fitted using the classical Curie-Weiss law [51]:

$$\frac{1}{\epsilon_r} = \frac{(T - T_0)}{C} \tag{1}$$

and the modified Curie-Weiss Law relation [50]:

$$\frac{1}{\epsilon_r} - \frac{1}{\epsilon_m} = \frac{(T - T_m)^\gamma}{C'} \tag{2}$$

where, T is the temperature, T_0 the Curie-Weiss temperature, the subscript 'm' refers to the maximum of the dielectric constant and the temperature at which this maximum is reached. γ is the diffuseness exponent ($\gamma = 1$ for normal ferroelectrics and $\gamma = 2$ for ideal relaxors [51–52]), and C and C' are the Curie and Curie-like constants, respectively.

The linear fits corresponding to the Curie-Weiss law are shown in Fig. 7a, and the extracted parameters are listed in Table 2. All compositions exhibit a deviation from ideal Curie-Weiss behavior near T_m, characteristic of diffuse and relaxor-like transitions. The difference between T_0 and T_m supports that the ferroelectric transition is progressive rather than abrupt, reflecting the coexistence of ferroelectric (O-T phase) and paraelectric (tungsten-bronze secondary phase) regions over a broad temperature interval.

On the other hand, the shift of T_0 with EAE content demonstrates that minor A-site stoichiometric variations significantly affect thermal stability of the ferroelectric phase; in particular, a moderate EAE (0.6 mol%), tends to stabilize the dielectric response, whereas a higher excess (0.8 mol%), introduces additional disorder that reduces T_0, suggesting a weakening of long-range dipolar correlations. Additionally, in Figure S1, wider dielectric peaks and strong dispersion with frequency are observed, which, together with the Curie constant values obtained from the slope of Fig. 7a), are characteristic of a ferroelectric with relaxor behavior, in accordance with previous reports in the literature [49, 51–54].

Table 2 shows the diffusivity exponents (γ) values for all investigated compositions. The obtained γ values range from 1.40 to 1.49, confirming the diffuse nature of the ferroelectric transition in KNLNT-BZ ceramics with controlled alkali non-stoichiometry. Notably, a reduction of γ to 1.40 is observed for the 0.6 mol% EAE composition, suggesting a partial decrease in structural disorder, which

may be associated with a more effective compensation of alkali vacancies. Meanwhile, the increase of γ to 1.49 for the 0.8 mol% EAE indicates a more relaxor behavior. This enhancement of diffuseness is associated with increased chemical disorder and the generation of stronger local random electric fields, which disrupt long-range ferroelectric correlations and promote the formation of dynamically fluctuating polar regions.

It is important to emphasize that the dielectric anomaly observed around 460 °C is associated from the presence of the tungsten-bronze secondary phase and is more pronounced in the sample without alkali excess. However, the relaxor behavior and diffuseness of the ferroelectric transition occurring at lower temperatures are primarily dominated by nanoscale chemical disorder within the perovskite matrix. In this context, the secondary phase mainly affects the loss mechanisms at high temperatures. At the same time, the diffusivity of the ferroelectric transition and the increase in the γ parameter are governed by local compositional fluctuations and the formation of polar nanoregions (PNRs) [50–53].

Therefore, to further elucidate the correlation between dielectric diffuseness and polarization dynamics, the ferroelectric response of the ceramics was therefore investigated in the following section through polarization-electric field (*P-E*) hysteresis measurements and fatigue analysis.

3.5 Ferroelectric hysteresis and fatigue behavior

Figure 8a shows the polarization vs. electric field (*P-E*) hysteresis loops of KNLNT-BZ with different EAE. A progressive increase in the coercive field (E_c) is observed with increasing alkali metal excess, which correlates with the reduction of paraelectric secondary phases and the improved stabilization of the perovskite ferroelectric matrix. At the same time, the remnant polarization (P_r), obtained from the hysteresis loops, increases from 6.2 to 7.7 $\mu C/cm^2$. This improvement is associated with the reduction and near elimination of the non-polar TB phase, resulting in a larger

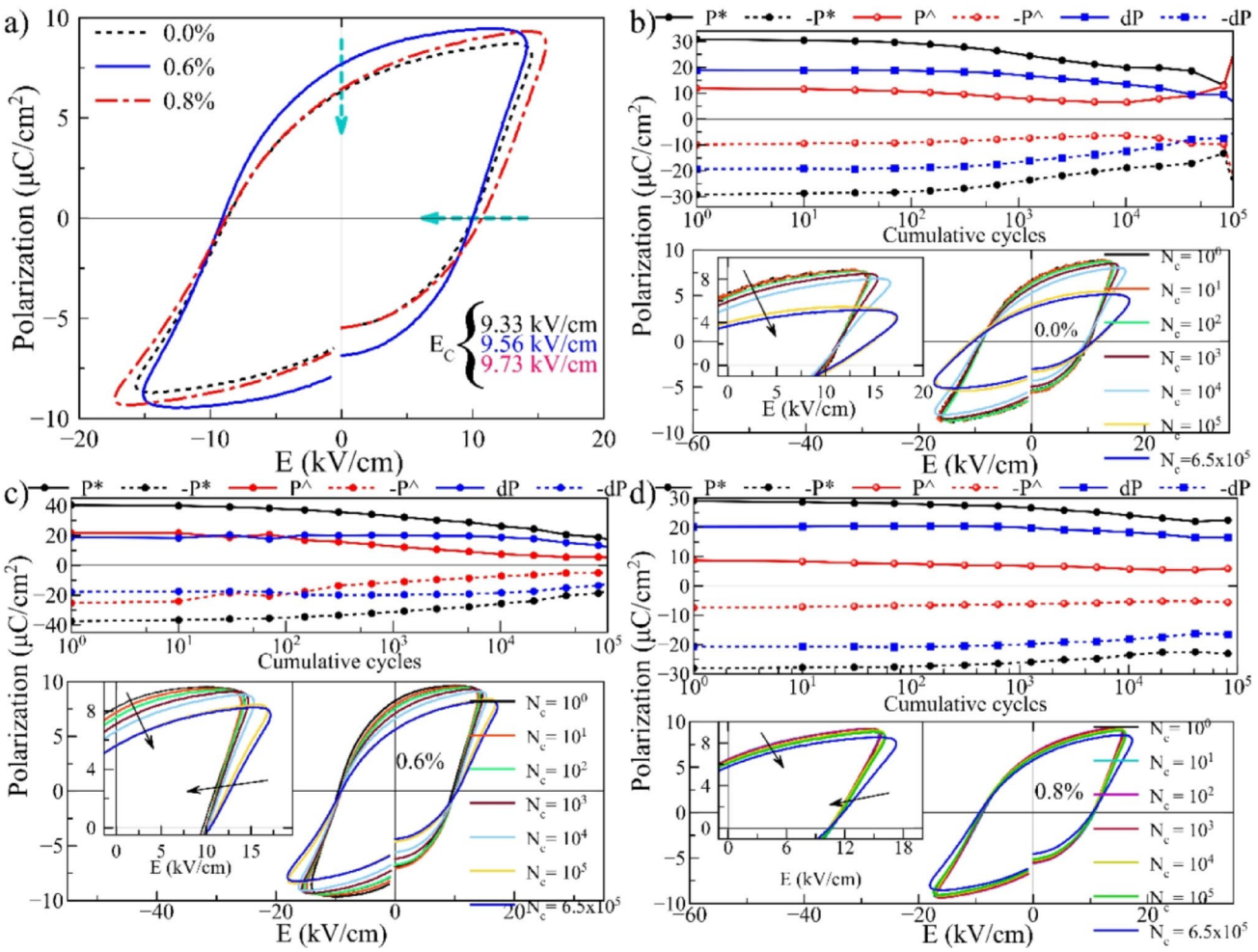


Fig. 8 (**a**) Polarization vs. electric field (P-E) hysteresis loops as a function of alkali excess, and Positive-up and Negative down (PUND) measurements of KNLNT-BZ containing (**b**) 0%, (**c**) 0.6%, and (**d**) 0.8 mol% EAE

effective ferroelectric volume fraction and enhanced polarization retention.

To evaluate the intrinsic switching behavior and eliminate non-switching and leakage contributions, Positive-Up Negative-Down (PUND) measurement was performed (Fig. 8b-d). The switched polarization was obtained as $\Delta P^{\pm} = P^{*}_{\pm} - P^{\wedge}_{\pm}$, (with $P^{*}_{\pm}$ as remnant+non-remnant polarization, and $P^{\wedge}_{\pm}$ as non-remnant polarization) and the remnant polarization was therefore calculated as $P_r = \frac{1}{4}(|\Delta P^{+}| + |\Delta P^{-}|)$. The P_r obtained from PUND are higher than those extracted directly from the conventional hysteresis loops, confirming that the correction effectively removes non-ferroelectric contributions such as leakage currents and dielectric displacement.

The evolution of the ferroelectric response under electrical cycling (Fig. 9) reveals distinct fatigue behaviors depending on alkali content. For the stoichiometric composition (0% EAE), both hysteresis loops (*P*-*E*) and P_r values exhibit pronounced degradation with increasing number of cycles, eventually approaching near-zero polarization. This fatigue behavior is attributed to the accumulation and redistribution of point defects, particularly alkali and oxygen vacancies, which are thermodynamically favored during high-temperature sintering. These defects generate internal bias fields that progressively pin ferroelectric domain walls, The pinning of domain walls suppresses reversible extrinsic contributions to polarization change and piezoelectric deformation [4, 22, 49]. Therefore, the degradation of the ferroelectric response in the stoichiometric composition can be associated not only with the reduction of the ferroelectric volume fraction due to the TB phase, but also with the reduction of domain wall mobility caused by the accumulation of defects, increasing the E_c and reducing the effective volume fraction of switchable domains, as observed in Fig. 8b. Consequently, the hysteresis loops shrink and become distorted, characteristic of a fatigued ferroelectric system.

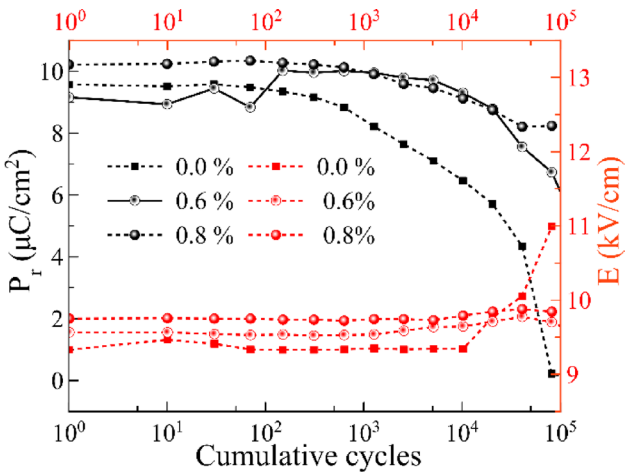


Fig. 9 Coercive field and remnant polarization as a function of the number of cycles. The remanent polarization extracted from PUND measurements was plotted as a single P_r value

In contrast, the 0.6 mol% EAE composition (Fig. 8c) shows significantly improved ferroelectric stability. The hysteresis loops retain their shape and area during cycling, and the degradation of P_r is markedly reduced compared to the stoichiometric sample. From a microscopic point of view, the moderate excess of alkali excess compensates for the volatilization-induced K/Na vacancies. As a result, ferroelectric switching proceeds through a more reversible and coherent domain nucleation and growth process. The domain mobility is reflected in reduced hysteresis loop asymmetry and a stable coercive field throughout the cycling process, that is consistent with recent reports on Ba-modified KNN systems, where two-step sintering has reduced the defect-mediated clamping [44], indicating effective suppression of fatigue mechanisms. The improvement in the hysteresis loop indicates that moderate alkali compensation facilitates more reversible domain wall movement, resulting from the reduction of local defect-induced pinning centers. Consequently, polarization switching becomes more homogeneous and energetically favorable.

For the 0.8 mol% EAE composition, the ferroelectric response becomes even more stable under repeated electrical cycling (Fig. 8d). This is evidenced by greater symmetry in the PUND measurements, minimal degradation of P_r and a stable E_c evolution. This enhanced stability can be associated with the increased structural disorder identified in the dielectric analysis, which is commonly linked to the emergence of polar nanoregions (PNRs) in relaxor ferroelectrics [50–53]. Therefore, ferroelectric switching is not governed solely by the long-range domain walls motion, but also by the induced alignment and reorientation of the PNRs, characteristic of relaxor-like ferroelectrics. The modified local chemistry appears to reduce the mobility of oxygen vacancies and other ionic carriers under alternating electric fields, thus minimizing charge injection, defect migration, and the consequent pinning of ferroelectric domains.

Therefore, while moderate alkali compensation (0.6 mol%) effectively reduces defect-induced fatigue by vacancy compensation, a slightly higher alkali excess (0.8 mol%) introduces controlled structural disorder that further enhances cycling stability through the stabilization of nanoscale polar entities and suppression of defect mobility. Since the piezoelectric response is intrinsically linked to ferroelectric domain dynamics, the implications of the observed polarization behavior on the piezoelectric properties are examined next.

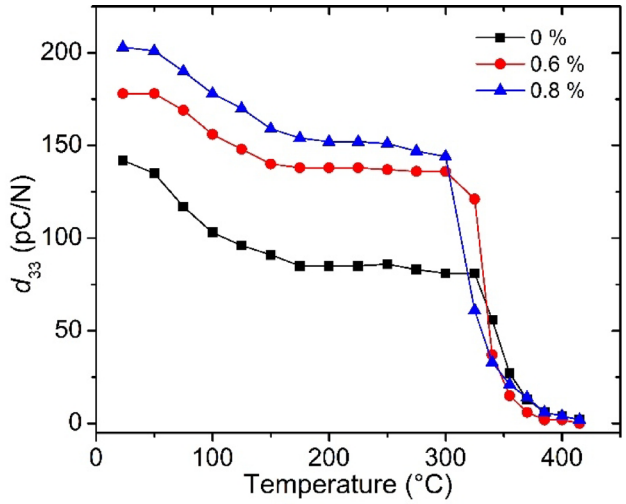


Fig. 10 Piezoelectric coefficient d_{33} as a function of temperature

3.6 Piezoelectric and electromechanical parameters

Figure 10 shows the temperature dependence of d_{33} coefficient for KNLNT-BZ ceramic with different alkali excess amounts. A moderate dependence is observed; specifically, the reduction of the non-polar secondary phase leads to a significant enhancement of d_{33} for compositions with higher EAE. This confirms that improving the perovskite phase purity directly benefits the microscopic piezoelectric response. From the domain structure point of view, the suppression of TB phase content and the reduction of crystalline defects, compensated by the excess alkali, also decrease the pinning effects of the domain walls, which enhances the reversible extrinsic contributions to the piezoelectric response; that is, the improvement in electromechanical coupling is associated not only with intrinsic polarizability, but also with greater mobility of the ferroelectric domain walls.

Thermally, the piezoelectric response shows an initial attenuation from room temperature up to the first structural transition (O-T). In this region, a reduction of approximately 34%, 20%, and 17% is observed for 0%, 0.8%, and 0.6% EAE compositions, respectively. After this transition, d_{33} remains relatively stable until approaching the Curie temperature, where it rapidly drops to zero, as expected for the ferroelectric-paraelectric transition. Importantly, no significant changes in d_{33} are observed near the high-temperature dielectric anomaly ($\sim 460\ ^{o}$C) associated with the TB secondary phase, confirming that this phase does not directly contribute to the piezoelectric response, in contrast to what has been observed in single-phase tungsten-bronze thin films [46]. The improved thermal stability observed for the 0.6 mol% EAE sample can be attributed to more effective vacancy compensation, which stabilizes domain configuration and limits thermally activated defect motion.

The room temperature piezoelectric and electromechanical parameters are summarized in Table 3. The impedance spectra used for determining the resonance and antiresonance frequencies employed in the calculation of k_p, k_{31} and related piezoelectric parameters are provided in the supplementary material (Fig. S3). The planar coupling factor k_p increases from 41.9% for the stoichiometric composition to 48.5% for the 0.6% EAE sample, followed by a slight reduction to 47.1% for 0.8% composition. This non-monotonic behavior indicates that moderate alkali excess optimizes electromechanical energy conversion efficiency through partial compensation of alkali vacancies, reduction of non-polar phases, and suppression of defect-induced domain walls pinning [55]. At 0.8 mol% EAE, the additional chemical disorder appears to counterbalance this benefit, leading to saturation or slight decrease of k_p.

A similar behavior is observed for the transverse coupling factor k_{31}, which reaches a maximum value of 29.1% at 0.6% excess and slightly decreases at 0.8% composition. Since k_{31} is strongly influenced by non 180° domain-wall motion [4, 49, 51], the enhancement observed at moderate alkali excess suggests improved lateral domain mobility and reduced defect-mediated clamping, thereby optimizing reversible extrinsic contributions associated with domain-wall displacement, while higher excess introduces local random fields that limit cooperative domain-wall motion.

In contrast, the thickness coupling factor k_t shows a monotonic increase with EAE content, reaching 43.3% for the 0.8% composition. This behavior indicates that longitudinal electromechanical coupling benefits from enhanced polarizability along the field direction, consistent with the mitigation of the TB phase and the significant increase in dielectric permittivity ϵ^{T}_{33} (799 for 0.8% EAE).

The transverse piezoelectric coefficient d_{31} increases in magnitude with alkali excess, reaching −75.1 pC/N for the 0.8 mol% composition. This enhancement reflects a smoother and more homogeneous polar response resulting from defect mitigation within the ferroelectric domains, as supported by the improved fatigue endurance and stable

Table 3 Piezoelectric parameters of KNLNT-BZ ceramics

Sample	k_p (%)	k_{31} (%)	k_t (%)	d_{31} (pC/*N*)	d_{33} (pC/*N*)	ε_{33}^{T}	g_{31} (10^{-3} m.V.N^{-1})	g_{33} (10^{-3} m.V.N^{-1})
0.0%	41.9	24.1	39.6	−58.4	142	652.5	−10.1	24.6
0.6%	48.5	29.1	42.4	-69.6	172	646.9	-12.1	29.9
0.8%	47.1	27.9	43.3	-75.1	203	799.0	-10.6	28.7

coercive field observed in the ferroelectric analysis. The suppression of defect-mediated pinning and charge migration allows dynamically active yet structurally stabilized polar states, as reported for defect-engineered KNN-based systems [10, 13, 50, 56], to contribute efficiently to the piezoelectric response.

Similarly, the longitudinal coefficient d_{33} increases monotonically with alkali excess, reaching 203 pC/N for the 0.8% composition. This behavior results from the combined effects of vacancy compensation, enhanced lattice polarizability, and improved domain-wall contributions. However, analysis of the piezoelectric voltage coefficient g_{31} and g_{33} reveals a maximum at 0.6% excess, followed by a slight decrease at 0.8%. Since $g_{ij} \propto d_{ij}/\epsilon_{ij}^{T}$, this behavior highlights the trade-off between piezoelectric charge sensitivity and dielectric permittivity. While high permittivity enhances strain response, it reduces voltage sensitivity. Therefore, the 0.6% composition is more favorable for sensor-type applications, where voltage output is critical.

Overall, these results confirm that alkali excess plays a dual role in tailoring the piezoelectric properties of KNLNT-BZ ceramics. A moderate excess (0.6%) optimizes electromechanical coupling and voltage sensitivity by balancing defect compensation and ferroelectric domain wall-mobility, whereas higher excess (0.8%) maximizes the absolute piezoelectric coefficients d_{31} and d_{33}, at the expense of increased dielectric softness and slightly reduced voltage response.

Although direct domain imaging was not performed in this work, the experimental results still provide indirect evidence of domain-wall-related contributions to the piezoelectric response, in agreement with previous reports for KNN-based ceramics [4, 22, 49, 51]. The increase in k_{31} at moderate alkali excess appears to be related to improved lateral domain-wall mobility, likely promoted by the reduction of the nonpolar TB phase and the lower concentration of defect-induced pinning centers. For the 0.8 mol% EAE composition, the slight decrease of k_{31} may indicate that stronger local random fields begin to partially restrict cooperative domain-wall motion, despite improving fatigue resistance. At the same time, the continuous increase in d_{33}, reaching 203 pC/N, suggests that both intrinsic lattice polarizability and reversible extrinsic contributions participate in the enhancement of the piezoelectric response. This interpretation is also consistent with the stable coercive field and the improved cycling stability observed in the hysteresis and PUND measurements.

4 Conclusions

The $0.96(K_{0.48}Na_{0.52})_{0.95}Li_{0.05}Nb_{0.95}Ta_{0.05}O_3$-$0.04BaZrO_3$ (KNLNT-BZ) piezoelectric ceramics were successfully synthesized via the conventional solid state, and their structural, dielectric, ferroelectric, and piezoelectric properties were systematically tailored through controlled alkali non-stoichiometry. The content of the tungsten-bronze secondary phase diminished from ~1.84 wt% in the stoichiometric composition to ~1.53 wt% with 0.6 mol% alkali excess and was almost completely suppressed at 0.8 mol% excess, confirming that additional alkali effectively compensates volatilization during sintering and stabilizes the perovskite matrix.

The suppression of the non-polar phase led to enhanced piezoelectric performance, with d_{33} increasing from 142 pC/N to 203 pC/N (0.8%). Moderate alkali excess (0.6%) optimized defect compensation and electromechanical coupling, while higher excess (0.8%) maximized piezoelectric coefficients through enhanced polarizability and relaxor-like contributions from polar nanoregions.

These results demonstrate that the precise stoichiometry control via alkali excess is a key strategy for balancing long-range ferroelectric order and relaxor characteristics in KNLNT-BZ ceramics. Controlled non-stoichiometry enables the optimization of phase purity, defect chemistry, and domain dynamics, providing an effective pathway for designing high-performance lead-free piezoceramics tailored to specific functional applications.

Supplementary Information The online version contains supplementary material available at https://doi.org/10.1007/s43207-026-00653-y.

Acknowledgements R. Lopez-Juárez thanks to *Dirección General de Asuntos del Personal Académico de la Universidad Nacional Autónoma de México* (DGAPA-UNAM) for financial support under project number PAPIIT-IN105325. E. Martinez-Aguilar and H'Linh Hmok thanks to *Secretaría de Ciencia, Humanidades, Tecnología e Innovación* (SECIHTI) for the postdoctoral fellowship No. 2022–2023. No. MOD.ORD.11/2025.

Author contributions E. Martínez-Aguilar contributed to the investigation, data curation, writing—original draft, writing—review & editing. O. Hernández-Cristóbal contributed to the Investigation and Data curation. H. Hmok was involved in formal analysis, and writing—original draft. R. López-Juárez was involved in the conceptualization, methodology, investigation, data curation, writing—original draft, writing—review & editing.

Funding This research was supported by DGAPA-UNAM under project number PAPIIT-IN105325.

Data availability All data generated or analyzed during this study are included in this published article.

Declarations

Conflict of interest The authors declare that they have no known competing financial interests or personal relationships that could have appeared to influence the work reported in this paper.

Open Access This article is licensed under a Creative Commons Attribution 4.0 International License, which permits use, sharing, adaptation, distribution and reproduction in any medium or format, as long as you give appropriate credit to the original author(s) and the source, provide a link to the Creative Commons licence, and indicate if changes were made. The images or other third party material in this article are included in the article's Creative Commons licence, unless indicated otherwise in a credit line to the material. If material is not included in the article's Creative Commons licence and your intended use is not permitted by statutory regulation or exceeds the permitted use, you will need to obtain permission directly from the copyright holder. To view a copy of this licence, visit http://creativecommons.org/licenses/by/4.0/.

References

1. H.C. Song, K.H. Cho, H.Y. Park, C.W. Ahn, S. Nahm, K. Uchino, S.H. Park, H.G. Lee, Microstructure and Piezoelectric Properties of (1-x)($Na_{0.5}K_{0.5}$)NbO_3–x$LiNbO_3$ Ceramics. J. Am. Ceram. Soc. **90**, 1812–1816 (2007)
2. G.H. Haertling, Ferroelectric Ceramics: History and Technology. J. Am. Ceram. Soc. **82**, 797–818 (1999)
3. K. Tsuji, Z. Fan, S.H. Bang, S. Dursun, S. Trolier-McKinstry, C.A. Randall, Cold sintering of the ceramic potassium sodium niobate, ($K_{0.5}Na_{0.5}$)NbO_3, and influences on piezoelectric properties. J. Eur. Ceram. Soc. **42**, 105–111 (2022)
4. European commission, Restriction of Hazardous Substances in Electrical and Electronic Equipment (RoHS), (2023). https://environment.ec.europa.eu/topics/waste-and-recycling/rohs-directive_en. Accessed 27 October 2025
5. K.C. Singh, C. Jiten, R. Laishram, O.P. Thakur, D.K. Bhattacharya, Structure and electrical properties of Li- and Ta-substituted $K_{0.5}Na_{0.5}NbO_3$ lead-free piezoelectric ceramics prepared from nanopowders. J. Alloy Compd. **496**, 717–722 (2010)
6. Z. Cen, Y. Zhen, W. Feng, P. Zhao, L. Chen, X. Wang, X.L. Li, Sintering temperature effect on microstructure, electrical properties and temperature stability of MnO-modified KNN-based ceramics. J. Eur. Ceram. Soc. **38**, 3136–3146 (2018)
7. Y. Cheng, J. Xing, T. Wang, F. Wang, R. Li, X. Sun, L. Xie, Z. Tan, J. Zhu, Realization of densified microstructure and large piezoelectricity in KNN ceramics via the addition of oxide additives. J. Mater. Sci. Mater. Electron. **32**, 20211–20224 (2021)
8. G. Ye, J. Wade-Zhu, J. Zou, T. Zhang, T.W. Button, J. Binner, Microstructures, piezoelectric properties and energy harvesting performance of undoped ($K_{0.5}Na_{0.5}$)NbO_3 lead-free ceramics fabricated via two-step sintering. J. Eur. Ceram. Soc. **40**, 2977–2988 (2020)
9. Y. Huang, X. Wang, Y. Ma, X. Lv, J. Wu, Multiscale understanding the effect of K/Na ratio on electrical properties of high-performance KNN-based ceramics. J. Am. Ceram. Soc. **107**, 355–366 (2024)
10. Y. Liu, J. Wu, T. Wang, T. Wei, Y. Huan, Mechanism for enhanced piezoelectric response in excess alkali metal doped KNN-based ceramics. J. Alloy Compd. **1036**, 181687 (2025)
11. T. Bongkarn, S. Chootin, S. Pinitsoontorn, S. Maensiri, Excellent piezoelectric and ferroelectric properties of KNLNTS ceramics with Fe_2O_3 doping synthesized by the solid-state combustion technique. J. Alloy Compd. **682**, 14–21 (2016)
12. R. López, F. González, M.P. Cruz, M.E. Villafuerte-Castrejón, Piezoelectric and ferroelectric properties of $K_{0.5}Na_{0.5}NbO_3$ ceramics synthesized by spray drying method. Mater. Res. Bull. **46**, 70–74 (2011)
13. Y. Cheng, W. Fan, H. Chen, L. Xie, J. Xing, Z. Tan, J. Zhu, Hardening Effect in Lead-Free KNN-Based Piezoelectric Ceramics with CuO Doping. ACS Appl. Mater. Interfaces. **14**, 55803–55811 (2022)
14. R. López-Juárez, V. Gómez-Vidales, M.P. Cruz, M.E. Villafuerte-Castrejón, Dielectric, Ferroelectric, and Piezoelectric Properties of Mn-Doped $K_{0.5}Na_{0.5}NbO_3$ Lead-Free Ceramics. J. Electron. Mater. **44**, 2862–2868 (2015)
15. E. Hollenstein, D. Damjanovic, N. Setter, Temperature stability of the piezoelectric properties of Li-modified KNN ceramics. J. Eur. Ceram. Soc. **27**, 4093–4097 (2007)
16. J. Gao, D. Xue, W. Liu, C. Zhou, X. Ren, Recent Progress on $BaTiO_3$-Based Piezoelectric Ceramics for Actuator Applications. Actuators. **6**, 24 (2017)
17. Z.Y. Shen, J.F. Li, Enhancement of piezoelectric constant d_{33} in $BaTiO_3$ ceramics due to nano-domain structure. J. Ceram. Soc. Jpn. **118**, 940–943 (2010)
18. Y. Zhu, Y. Zhang, B. Xie, P. Fan, M.A. Marwat, W. Ma, C. Wang, B. Yang, J. Xiao, H. Zhang, Large electric field-induced strain in $AgNbO_3$-modified 0.76$Bi_{0.5}Na_{0.5}TiO_3$-0.24$SrTiO_3$ lead-free piezoceramics. Ceram. Int. **44**, 7851–7857 (2018)
19. W. Bai, D. Chen, Y. Huang, B. Shen, J. Zhai, Z. Ji, Electromechanical properties and structure evolution in $BiAlO_3$-modified $Bi_{0.5}Na_{0.5}TiO_3$-$BaTiO_3$ lead-free piezoceramics. J. Alloy Compd. **667**, 6–17 (2016)
20. H. Wang, X. Zhai, J. Xu, X. Zhao, L. Yang, Influence on structure and properties of CuO addition to KNN–LS–BF piezoelectric ceramics. J. Mater. Sci. Mater. Electron. **27**, 5016–5019 (2016)
21. Y. Ding, Z. Tan, Y. Pan, Y. Wang, Y. Dong, W. Liu, T. Zheng, J. Wu, Revealing the Origin of Property Discrepancy in KNN-Based Ceramics with Extreme K/Na Ratio for Sensing Application. Small. **21**, 2502418 (2025)
22. Z. Fu, J. Yang, P. Lu, L. Zhang, H. Yao, F. Xu, Y. Li, Influence of secondary phase on polymorphic phase transition in Li-doped KNN lead-free ceramics. Ceram. Int. **43**, 12893–12897 (2017)
23. Y. Guo, K. Kakimoto, H. Ohsato, Phase transitional behavior and piezoelectric properties of ($Na_{0.5}K_{0.5}$)NbO_3-$LiNbO_3$ ceramics. Appl. Phys. Lett. **85**, 4121–4123 (2004)
24. M.M. Ftini, B. Ayed, A. Haddad, $K_{2.6}Nb_{11.6}O_{30}$: a novel tetragonal bronze structure. J. Chem. Crystallogr. **33**, 123–129 (2003)
25. Y. Wang, D. Damjanovic, N. Klein, E. Hollenstein, N. Setter, Compositional Inhomogeneity in Li- and Ta-Modified (K,Na)NbO_3 Ceramics. J. Am. Ceram. Soc. **90**, 3485–3489 (2007)
26. Y. Zhang, L. Li, B. Shen, J. Zhai, Effect of orthorhombic–tetragonal phase transition on structure and piezoelectric properties of KNN-based lead-free ceramics. Dalton Trans. **44**, 7797 (2015)
27. J. Liu, J. Zhu, M. Wang, Y. Pu, X. Li, P. Sun, L. Feng, X. Zhu, J. Zhu, D. Xiao, Effects of K/Na ratio on the phase structure and electrical properties of 0.98(K_xNa_{1-x})NbO_3–0.02$BiScO_3$ lead-free ceramics. Ceram. Int. **38S**, S347–S350 (2012)
28. Y. Zhen, J.F. Li, K. Wang, Y. Yan, L. Yu, Spark plasma sintering of Li/Ta-modified (K,Na)NbO_3 lead-free piezoelectric ceramics: Post-annealing temperature effect on phase structure, electrical properties and grain growth behavior. Mater. Sci. Eng. B **176**, 1110–1114 (2011)
29. R. López-Juárez, F. González-García, J. Zárate-Medina, R. Escalona-González, S. Díaz, de la M.E. Torre, Villafuerte-Castrejón, Piezoelectric properties of Li–Ta co-doped potassium–sodium niobate ceramics prepared by spark plasma and conventional sintering. J. Alloy Compd. **509**, 3837–3842 (2011)

30. C. Wang, B. Fang, Y. Qu, Z. Chen, S. Zhang, J. Ding, Preparation of KNN based lead-free piezoelectric ceramics via composition designing and two-step sintering. J. Alloy Compd. **832**, 153043 (2020)
31. J. Ji, X. Li, B. Fang, X. Zhao, S. Zhang, J. Ding, H. Luo, Improving densification and electrical properties of KNN-based lead-free piezoceramics via two-step sintering method. Ferroelectrics. **526**, 33–45 (2018)
32. L. Karacasulu, C. Vakifahmetoglu, Cold sintering assisted two-step sintering of potassium sodium niobate (KNN) ceramics. Mater. Sci. Eng. B **297**, 116709 (2023)
33. S. Supriya, Cold sintering, microstructure and dielectric–ferroelectric anomalies of lead–free $K_{0.5}Na_{0.5}NbO_3$ ceramics. J. Mater. Sci. **60**, 13294–13313 (2025)
34. Z. Cen, Z. Dong, Z. Xu, F.Z. Yao, L. Guo, L. Li, X. Wang, Improving fatigue properties, temperature stability and piezoelectric properties of KNN-based ceramics via sintering in reducing atmosphere. J. Eur. Ceram. Soc. **41**, 4462–4472 (2021)
35. V.A. Balanov, Z. Zhao, M. Pan, A. Feldhoff, Y. Bai, Sol–gel synthesis and structural characterization of band gap engineered ferroelectric perovskite oxide potassium sodium barium nickel niobate. J. Sol-Gel Sci. Technol. **96**, 649–658 (2020)
36. G.H. Khorrami, A. Kompany, A.K. Zak, A facile sol–gel approach to synthesize KNN nanoparticles at low temperature. Mater. Lett. **110**, 172–175 (2013)
37. F. Zhang, L. Han, S. Bai, T. Sun, T. Karaki, M. Adachi, Hydrothermal Synthesis of (K,Na)NbO_3 Particles. Jpn J. Appl. Phys. **47**, 7685–7688 (2008)
38. R. López-Juárez, R. Castañeda-Guzmán, M.E. Villafuerte-Castrejón, Fast synthesis of $NaNbO_3$ and $K_{0.5}Na_{0.5}NbO_3$ by microwave hydrothermal method. Ceram. Int. **40**, 14757–14764 (2014)
39. Y. Shiratori, A. Magrez, C. Pithan, Particle size effect on the crystal structure symmetry of $K_{0.5}Na_{0.5}NbO_3$. J. Eur. Ceram. Soc. **25**, 2075–2079 (2005)
40. C. Alemany, L. Pardo, B. Jiménez, F. Carmona, J. Mendiola, A.M. González, Automatic Iterative Evaluation of Complex Material Constants in Piezo-electric Ceramics. J. Phys. D: Appl. Phys. **27**, 148–155 (1994)
41. M. Algueró, C. Alemany, L. Pardo, A.M. González, Method for obtaining the full set of linear electric, mechanical, and electromechanical coefficients and all related losses of a piezoelectric ceramic. J. Am. Ceram. Soc. **87**, 209–215 (2004)
42. O. Arcelus, J. Rodríguez-Carvajal, N.A. Katcho, M. Reynaud, A.P. Black, D. Chatzogiannakis, C. Frontera, J. Serrano-Sevillano, M. Ismail, J. Carrasco, F. Fauth, M.R. Palacin, Casas-Cabanas, FullProfAPP: a graphical user interface for the streamlined automation of powder diffraction data analysis. J. Appl. Cryst. **57**, 1676–1690 (2024)
43. Y. Liu, J. Fan, X. Qi, B. Shen, R. Zhang, K. Yao, Adaptive ferroelectric states in KNN-based piezoceramics: Unveiling the mechanism of enhancing piezoelectric properties through multiple phase boundary engineering. Nano Energy. **128**, 109972 (2024)
44. Z. Yang, Y. Fan, Y. Jia, X. Chen, K. Shang, S. Tang, H. Fan, W. Wang, Thermal and electromechanical performance in $BaSnO_3$-modified potassium sodium niobate piezoceramics via two-step sintering. Ceram. Int. **50**, 42237–42246 (2024)
45. R. Neurgaonkar, L.E. Cross, Piezoelectric tungsten bronze crystals for saw device applications. Mater. Res. Bull. **21**, 893–899 (1986)
46. B. Allouche, Y. Gagou, A. Belboukhari, F.L. Marrec, M.E. Marssi, Structural and electrical properties of $K_3Li_2Nb_5O_{15}$ thin film grown by pulsed laser deposition. Mater. Res. Bull. **94**, 287–290 (2017)
47. R.M. German, P. Suri, S.J. Park, Review: liquid phase sintering. J. Mater. Sci. **44**, 1–39 (2009)
48. W. Xiaoyong, F. Yujun, Y. Xi, Dielectric relaxation behavior in barium stannate titanate ferroelectric ceramics with diffused phase transition. Appl. Phys. Lett. **83**, 2031–2033 (2003)
49. P. Li, J. Zhai, B. Shen, S. Zhang, X. Li, F. Zhu, X. Zhang, Ultrahigh Piezoelectric Properties in Textured (K,Na)NbO_3-Based Lead-Free Ceramics. Adv. Mater. **30**, 1705171 (2018)
50. C.W. Cho, M.R. Cha, J.Y. Jang, S.H. Lee, D.J. Kim, S. Park, J.S. Bae, S.D. Bu, S. Lee, J. Hu, Ferroelectric relaxor properties of $(1\text{-}x)K_{0.5}Na_{0.5}NbO_3\text{-}xBa_{0.5}Ca_{0.5}TiO_3$ ceramics. Curr. Appl. Phys. **12**, 1266–1271 (2012)
51. M.E. Lines, A.M. Glass, Principles and Applications of Ferroelectrics and Related Materials (Oxford University Press, 1977)
52. K. Uchino, S. Nomura, Critical exponents of the dielectric constants in diffuse-phase-transition crystals. Ferroelectrics. **44**, 55–61 (1982)
53. T.A. Duong, F. Erkinov, M. Aripova, C.W. Ahn, B.W. Kim, H.S. Han, J.S. Lee, Ferroelectric–to–relaxor crossover in KNN–based lead–free piezoceramics. Ceram. Int. **47**, 4925–4932 (2021)
54. A. Włódarkiewicz, M.E. Costa, P.M. Vilarinho, The dissolution of potassium sodium niobate (KNN) in aqueos media towards sustainable electroceramics sintering. Mater. Des. **233**, 112169 (2023)
55. L. Duan, X. Zhang, T. Xu, A. Zhang, Y. Wei, J. Guo, Z. Xu, G. Li, R. Chu, Er-doped $0.96(K_{0.48}Na_{0.52})(Nb_{0.965}Sb_{0.035})O_3\text{-}0.04(Bi_{0.5}Na_{0.5})ZrO_3$ Multifunctional Ceramics with Good Temperature Stability. J. Electron. Mater. **53**, 5663–5670 (2024)
56. Y. Dai, X. Zhang, G. Zhou, Phase transitional behavior in $K_{0.5}Na_{0.5}NbO_3$–$LiTaO_3$ ceramics. Appl. Phys. Lett. **90**, 262903 (2007)

Publisher's Note Springer Nature remains neutral with regard to jurisdictional claims in published maps and institutional affiliations.